# Lifetime, Mobility, and Diffusion of Photoexcited Carriers in Ligand-Exchanged Lead Selenide Nanocrystal Films Measured by Time-Resolved Terahertz Spectroscopy

Glenn W. Guglietta,[†,⊥] Benjamin T. Diroll,[‡,⊥] E. Ashley Gaulding,[§] Julia L. Fordham,[§] Siming Li,[†] Christopher B. Murray,*[,‡,§] and Jason B. Baxter*[,†]

[†]Department of Chemical and Biological Engineering, Drexel University, 3141 Chestnut Street, Philadelphia, Pennsylvania 19104, United States, [‡]Department of Chemistry, University of Pennsylvania 231 South 34th Street, Philadelphia, Pennsylvania 19104, United States, and [§]Department of Materials Science, University of Pennsylvania, 3231 Walnut Street, Philadelphia, Pennsylvania 19104, United States. [⊥]G. W. Guglietta and B. T. Diroll contributed equally.

ABSTRACT Colloidal semiconductor nanocrystals have been used as building blocks for electronic and optoelectronic devices ranging from field-effect transistors to solar cells. Properties of the nanocrystal films depend sensitively on the choice of capping ligand to replace the insulating synthesis ligands. Thus far, ligands leading to the best performance in transistors result in poor solar cell performance, and *vice versa*. To gain insight into the nature of this dichotomy, we used time-resolved terahertz spectroscopy measurements to study the mobility and lifetime of PbSe nanocrystal films prepared with five common ligand-exchange reagents. Noncontact terahertz
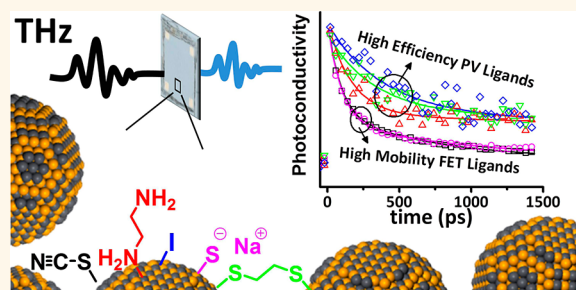
spectroscopy measurements of conductivity were corroborated by contacted van der Pauw measurements of the same samples. The films treated with different displacing ligands show more than an order of magnitude difference in the peak conductivities and a bifurcation of time dynamics. Inorganic chalcogenide ligand exchanges with sodium sulfide (Na_2S) or ammonium thiocyanate (NH_4SCN) show high mobilities but nearly complete decay of transient photocurrent in 1.4 ns. In contrast, ligand exchanges with 1,2-ethylenediamine (EDA), 1,2-ethanedithiol (EDT), and tetrabutylammonium iodide (TBAI) show lower mobilities but longer carrier lifetimes, resulting in longer diffusion lengths. This bifurcated behavior may explain the divergent performance of field-effect transistors and photovoltaics constructed from nanocrystal building blocks with different ligand exchanges.

KEYWORDS: terahertz spectroscopy · lead selenide · quantum dots · solar cells · photoconductivity · field-effect transistors · THz

Colloidal nanocrystals (NCs) are a popular emerging building block for solution-processed electronics, including thin-film transistors[1,2] and circuits,[3,4] photodetectors,[5−7] light-emitting diodes,[8−10] and photovoltaics.[5,11] In most cases, NCs are synthesized in nonpolar organic solvents and stabilized by aliphatic ligands (*e.g.*, oleic acid), which are removed or replaced to enhance charge transport between NCs in the solid state.[12] This approach has generated materials with performance comparable to or better than other emerging thin-film materials, including field-effect mobilities of $>30\ cm^2\ V^{-1}\ s^{-1}$ or photovoltaic power conversion efficiencies of $>8.5\%$.[4,13]

However, the chemical pathway from insulating NC solids capped with aliphatic ligands to high-performance NC solids differs substantially depending on the end application and the relevant figure of merit. In particular, those ligand-exchange strategies that lead to state-of-the-art photovoltaic performance commonly show typical field-effect mobilities orders of magnitude lower than the best NC field-effect transistors (FETs). The converse comparison is even more stark: none of the ligand-exchange strategies yielding NC solids with mobilities above $10\ cm^2\ V^{-1}\ s^{-1}$ have yet demonstrated measurable photovoltaic efficiencies. Recently, Zhitomirsky *et al.* have argued that

present limitations for NC solar cells arise from high trap state density in NC films, which dictates that increases in mobility offer negligible return in photovoltaic performance.[14] We used time-resolved photoconductivity measurements to analyze this problem.

Time-resolved terahertz spectroscopy (TRTS) uses a noncontact, ac probe to measure the dynamics of sample photoconductivity, providing additional and complementary information compared to contacted device measurements.[15,16] TRTS probes transient local conductivity on subpicosecond to nanosecond time scales that are relevant to carrier dynamics in semiconductor NC films. In our experiments, a pump pulse above the band gap energy is followed at variable delay times by a terahertz probe wave packet. The additional charge carriers generated by the pump pulse attenuates the terahertz probe by an amount proportional to the photoconductivity of the sample. TRTS and the related technique of time-resolved microwave conductivity (TRMC) have been applied to quantum dot films in a number of instances previously to examine ultrafast carrier relaxation (<10 ps) and longer-lived photocurrent.[17−26]

We performed TRTS measurements on PbSe NC films that were treated with five different ligand exchanges: sodium sulfide (Na_2S), ammonium thiocyanate (NH_4SCN), 1,2-ethylenediamine (EDA), 1,2-ethanedithiol (EDT), and tetrabutylammonium iodide (TBAI). This list of ligand exchanges captures a cross-section of literature strategies used in state-of-the-art transistors and photovoltaics. To compare TRTS with contacted electrical measurements, we performed the TRTS measurement within a van der Pauw pattern of electrodes. We find that Na_2S and NH_4SCN show higher conductivities but shorter lifetimes, whereas EDA, EDT, and TBAI show lower conductivities but longer lifetimes, resulting in longer diffusion lengths. These results help to elucidate the divergent nature of performance improvements in transistors with Na_2S and NH_4SCN treatments and in photovoltaics with EDT and TBAI treatments.

RESULTS AND DISCUSSION

TRTS Photoconductivities, Mobilities, and Time Dynamics. For TRTS measurements, NC films were fabricated air-free using layer-by-layer spin-coating and ligand exchange. The different ligand-exchange processes used in this paper were chosen to reflect various strategies for fabricating high-performance NC-based electronic devices. Na_2S and NH_4SCN are used in high-performance transistors of lead and cadmium chalcogenides.[27−32] EDA provides a more direct comparison with TRTS measurements of Murphy et al.[17] and TRMC measurements.[22,24] EDT and TBAI were chosen because they are popular ligands in high-performance PbE photovoltaics.[13,33,34]

Figure 1a shows the near-infrared (NIR) absorption spectra of the five thin-film samples with a solution-phase absorption measurement of the as-synthesized 5.5 nm PbSe NCs (see Supporting Information Figure S1). Ligand-exchanged films show broadening and a red-shift of the 1s excitonic absorption, typically attributed to increased interparticle coupling and increased dielectric constant, and a decrease of the intensity of hydrocarbon stretches at 3400 nm relative to the 1s absorption, reflecting displacement of oleic acid.[35] Repeating layer-by-layer deposition between 3 and 9 times resulted in films that were between 250 and 700 nm, as measured by atomic force microscopy (see Supporting Information Table S1 and Figures S2 and S3). In all cases, the optical density of the films
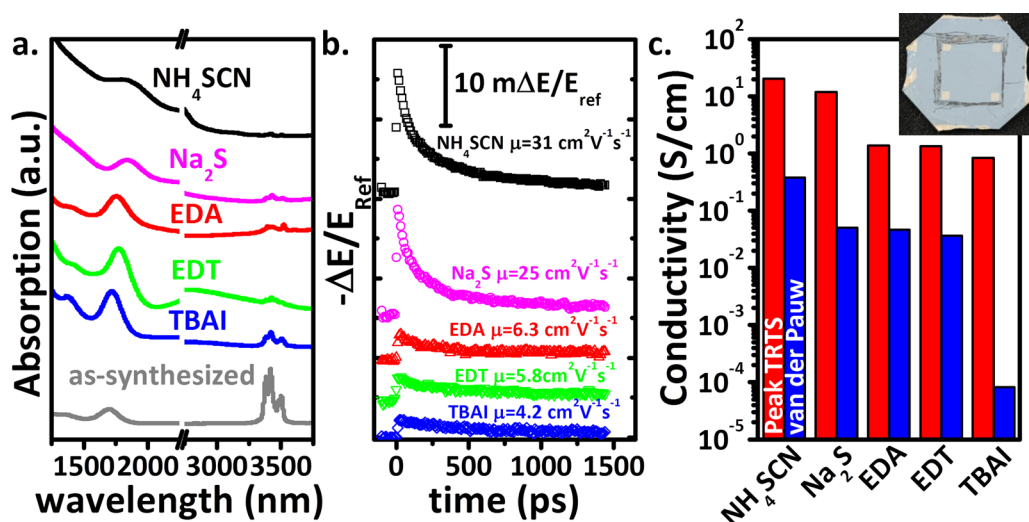

Figure 1. (a) NIR absorption spectra of the as-synthesized PbSe NCs in solution and NH_4SCN, Na_2S, EDA, EDT, and TBAI ligand-exchanged films. The data are offset vertically. (b) Data from TRTS photoconductivity measurements of ligand-exchanged films, scaled by the terahertz reference. Peak mobility values calculated from these data are reported next to each of the curves. (c) Peak TRTS photoconductivities (red bars) and van der Pauw conductivities (blue bars). Inset is a photograph of the van der Pauw substrate with square electrode patterns at 5 mm spacings.

exceeds 1.5 at the pump wavelength (720 nm), ensuring nearly complete absorption of the pump pulse. Although optically smooth, low-magnification SEM images do show cracking of the films (Supporting Information Figures S4 and S5), which may cause divergence of long-range (contacted) and short-range (e.g., TRTS) measures of conductivity. Small-angle X-ray scattering measurements (Supporting Information Figure S6) show that NCs in all cases are close-packed glasses, with substantial interparticle necking in the cases of Na$_2$S and NH$_4$SCN, similar to literature observations.[36−38]

Carrier dynamics were examined by TRTS using methods and analysis similar to those previously reported.[16,17,39,40] The photoexcited change in the terahertz electric field, measured at the peak of the difference signal in the time domain and at pump−probe delay time t_p, termed $\Delta E(t_p)$, is related to the sample photoconductivity according to eq 1:

$$\sigma(t_p) = -\frac{\Delta E(t_p)}{E_{ref}} \times \frac{2n_{eff}c\varepsilon_0}{d(t_p)} \quad (1)$$

in which E_{ref} is the magnitude of the electric field of the terahertz reference pulse, n_{eff} is the effective refractive index determined following literature procedures (see Supporting Information),[17] c is the speed of light, ε_0 is the permittivity of free space, and $d(t_p)$ is the photoexcited sample thickness, which varies with time depending on the diffusion of photoexcited carriers.[41] To determine an appropriate $d(t_0)$ to estimate the peak conductivities and sample mobilities, we first determined an empirical extinction coefficient at the pump wavelength for each film. Extinction coefficients for different exchanges varied from $\epsilon = 7.0 \times 10^4$ cm^{-1} to $\epsilon = 2.5 \times 10^5$ cm^{-1} (base e), which is consistent with the predicted extinction cross section and which varies in qualitative agreement with the index of the ligand environment (Supporting Information Figure S7).[42] Because we do not directly account for scattering and reflection losses ($\sim$10% when measured, see Supporting Information Figure S8), the empirical extinction coefficients are upper bounds. In our experiments, we assume that every absorbed photon generates one electron−hole pair and that electrons and holes, which have similar reported mobilities,[43] both contribute to the conductivity. Measurements of films without ligand exchange (Supporting Information Figure S9) confirm that the measured TRTS signal arises from inter-NC transport and not intra-NC conductivity. To estimate conductivity and mobility from TRTS measurements, we define $d(t_0)$ to be three times the skin depth ($3/\epsilon$). $d(t_0)$ is in the range of a few hundred nanometers (see Supporting Information Table S1). The total carrier density averaged over this photoexcited slab is calculated as $N = 2(1 - e^{-3})I_0/d(t_0)$, where I_0 is the incident flux. Across the samples, the carrier concentration we estimate varies from 1.2×10^{18} cm^{-3} to 4.0×10^{18} cm^{-3} and the average

number of excitons per NC varies from $\sim$0.2 to $\sim$0.6. We found that the sample response was weakly power-dependent in a manner inconsistent with Auger recombination (see Supporting Information Figure S10 and discussion below). In contrast, previous work by Murphy et al. used much higher pump powers and observed faster kinetics that were dominated by Auger recombination.[17]

Figure 1b shows the traces of $\Delta E(t_p)/E_{ref}$ for the PbSe NC films treated with the five different ligand exchanges, where the magnitude of the signal is proportional to the photoconductivity. In each case, photoconductivity rises with instrument-limited response and then decays over hundreds of picoseconds to nanoseconds. Carrier mobilities at the peak of the terahertz conductivity are also shown for each film, spanning a range of 4.2 cm^2 V^{-1} s^{-1} to 31.3 cm^2 V^{-1} s^{-1}. Mobilities are estimated according to $\mu \cong \sigma/qN$, where σ is the photoconductivity, q is the elementary charge, and N is the total photocarrier density calculated as described above. This experiment cannot distinguish carrier type in PbSe, so the reported mobility is the average mobility of the electron and hole.[22,24,44] The mobility calculated from our data for the same ligand treatment (EDA) falls below those measured by Murphy et al. using TRTS by a factor of 8. However, they interpreted TRTS with a photoexcited sample thickness of 2.2 μm, which lowers the apparent carrier density and raises the estimated mobility at a given photoconductivity. Furthermore, Murphy et al. estimated mobility of the NC network rather than the effective mobility of the thin film, which is more directly applicable to devices. Our mobility values for EDA- and EDT-exchanged PbSe NC films are above those measured by using TRMC.[22,24] TRMC shows lower mobilities than the TRTS measurements at least in part because the mobilities are measured with lower time resolution and are closer in frequency to dc measurements.

The NC films were patterned with four-point contacts for van der Pauw measurements spaced at a distance of 5 mm so that TRTS measurements could be performed on the same region of the same film, as shown in the inset of Figure 1c. Figure 1c plots the peak TRTS photoconductivities for each of the samples (red) and the conductivity of the samples measured using a van der Pauw measurement (blue). The dark van der Pauw conductivities and TRTS peak conductivities show the same trend: NH$_4$SCN > Na$_2$S > EDA > EDT > TBAI. Particularly in the TRTS measurement, the conductivities are primarily functions of the different mobilities, because the initial photoexcited carrier density is very similar across all samples. As expected, TRTS measurements show conductivities that are 1−2 orders of magnitude higher than van der Pauw measurements, largely because of the high density of carriers generated by photoexcitation. Additionally, mobilities measured by TRTS are expected to be larger
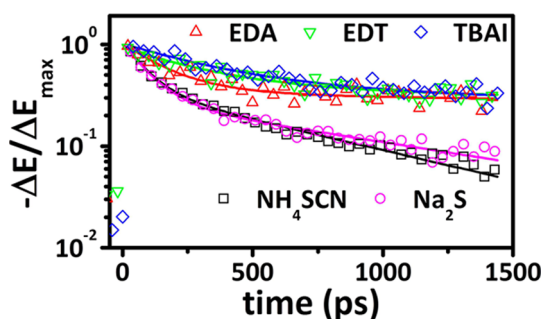
Figure 2. Normalized TRTS photoconductivity for each of the five ligand-exchanged samples plotted with solid fit lines of the same color. Some data points have been removed for visual clarity.

TABLE 1. Tabulated Fit Parameters of Ligand-Exchanged PbSe NC Films with Uncertainties

sample	A_1	t_1 [ps]	A_2 or A_∞	t_2 [ps]
NH$_4$SCN	0.70 (0.01)	87 (3)	0.36 (0.01)	728 (17)
Na$_2$S	0.76 (0.01)	97 (3)	0.28 (0.01)	1074 (51)
EDA	0.70 (0.03)	166 (12)	0.34 (0.01)	>10 ns
EDT	0.70 (0.03)	170 (21)	0.33 (0.03)	>10 ns
TBAI	0.67 (0.02)	384 (37)	0.35 (0.02)	>10 ns

than contacted measurements of mobility because TRTS is a *local* conductivity measurement that is less affected by imperfections in film morphology.[45,46] To separate the effects of carrier density and mobility in comparing TRTS and van der Pauw conductivities, Hall measurements were performed on the NH$_4$SCN-exchanged sample, yielding a hole density of 4×10^{17} cm^{-3} and a Hall mobility of 5.5 cm^2 V^{-1} s^{-1}. This mobility is comparable to earlier reports for PbSe nanocrystals,[47] but is significantly less than the 31 cm^2 V^{-1} s^{-1} measured by TRTS. Thus, for the NH$_4$SCN-exchanged sample, the photocarrier density is responsible for roughly 1 order of magnitude enhanced conductivity, and the higher TRTS mobility accounts for roughly a factor of 5 higher conductivity. Reliable dc Hall measurements on other films were not obtained due to low carrier mobility and unstable Hall voltages, but similar on/off ratios of EDT, EDA, and Na$_2$S (on/off ≈ 10−100) are reasonable based upon transistor measurements.[29,48−50] The TBAI film had a van der Pauw conductivity that was 4 orders of magnitude different than the TRTS value, a much greater difference than with the other exchanges. TBAI films may be subject to both lower carrier density and a more cracked structure compared to other films (see Supporting Information Figures S5a and S5b), both of which reduce the van der Pauw conductivity without affecting the TRTS probe of local photoconductivity.

Time- and Frequency-Resolved Conductivity. Figure 2 shows normalized TRTS scans of $\Delta E(t_p)/\Delta E_{max}$ to facilitate comparison of the distinct time dynamics of the samples. NH$_4$SCN- and Na$_2$S-exchanged samples show similar decays of 95% after 1.4 ns. In contrast, EDA, EDT, and TBAI have much slower kinetics, with about 30% of the signal remaining at 1.4 ns. Each of the data sets in Figure 2 is fitted with a biexponential curve shown as a solid line of the same color as the points. Values of the fitted parameters are reported in Table 1. Due to the flattening of the TRTS curves of the EDA-, EDT-, and TBAI-treated samples, there is a great deal of uncertainty in the slow time constant, which is clearly beyond the available temporal window. The data of those three samples can

alternatively be fit with a single exponential decay and a baseline offset (A_∞), implying $t_2 > 10$ ns.

TRTS decays can be interpreted under two limits, depending on the mechanism by which photoconductivity decays: either trapping or recombination of carriers. In the trapping limit, the decay in photoconductivity is due to reduction of charge carrier mobility $\mu(t)$. As carriers relax in energy, they move from energies with a high density of states to the band-edge or even trap states within the band gap that have a low density and consequently low mobility.[51] In the recombination limit, electron−hole recombination decreases conductivity by lowering the carrier concentration. Both are likely to occur simultaneously in NC solids (*e.g.*, trap-mediated recombination). Here, we assume that the decrease in photoconductivity is well-modeled by the recombination of electron−hole pairs because carrier relaxation is rapid[21,52] and both recombination and trapping of charge carriers—removal from high-mobility states—have similar results on the *effective* carrier concentration and the terahertz transmission.

The microscopic pathways of recombination in ligand-exchanged PbSe NC solids are potentially diverse. Although this work specifically targets an excitation flux that generates less than one exciton per NC, previous reports have claimed that Auger recombination is operative even at densities of less than 10^{-3} excitons/NC.[53] Detailed power-dependent studies are not the primary subject of this work, but time-dependent conductivity data for several powers are shown in Figure S10. The power dependence of the time-resolved conductivity allows some conclusions about the operative recombination mechanisms observed in our work. First-order processes (that is, dN/d$t \propto N$), like Shockley−Read−Hall, show no power dependence, whereas second- (*e.g.*, radiative recombination) or third-order processes (*e.g.*, Auger) have predictable power dependence, discussed in more detail in the Supporting Information. At long times, >1 ns, decays are power-independent, suggesting a trap-assisted recombination mechanism. At earlier times, we exclude Auger as a major recombination pathway in our work because the time-dependent signal collected at several powers is inconsistent with Auger recombination. We also note that the fastest time constant we observe (87 ps) is still much slower than reported Auger rates (<50 ps).[17,53]
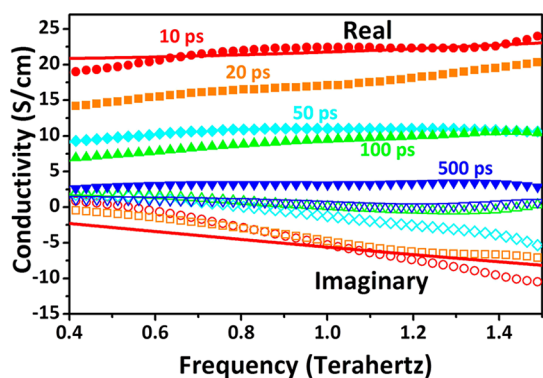
Figure 3. Experimental complex photoconductivity from TRTS measurements (points) fitted with a Drude–Smith model of photoconductivity (lines) at a 10 ps pump–probe delay time. Solid shapes represent the real conductivity, and open shapes represent the imaginary conductivity. Colors correspond to the pump–probe delay time.

We performed frequency-resolved photoconductivity experiments to evaluate our approximations of mobility and study the transport behavior in NC solids of high mobility. The full complex-valued frequency-dependent transient photoconductivity data are taken by probing the change in transmitted time-domain terahertz wave packet, $\Delta E(t,t_p)$, at different t_p delay times. A Fourier transform of the time-domain data and application of eq 1 enables calculation of the frequency-resolved complex photoconductivity $\sigma(\omega)$. Signal-to-noise considerations limited our ability to perform this experiment to the most conductive sample (NH$_4$SCN-exchanged). The real (closed point) and imaginary (open points) photoconductivity of the NH$_4$SCN-exchanged sample at different delay times is plotted in Figure 3. The sample shows behavior previously observed in NC films.[17,18,54,55] The real photoconductivity is positive and increases with frequency, while the amplitude decreases with increasing pump–probe delay as mobile carriers become trapped or recombine. The imaginary photoconductivity is negative, indicating localized transport, and similarly decreases in magnitude with pump–probe delay.

A number of models show frequency dependence that matches the general trends seen in Figure 3, including hopping and effective medium models for composites, plasmonic or excitonic models for homogeneous materials, and the Drude–Smith model that includes preferential backscattering.[56] To compare carrier density and mobility from the full frequency-dependent data to those calculated with the assumptions described in relation to Figure 1b, the real and imaginary conductivities at 10 ps were fit simultaneously by the truncated Drude–Smith model[57] shown in eq 2:

$$\sigma(\omega) = \frac{\varepsilon_0 \omega_p^2 \tau}{1 - i\omega\tau}\left(1 + \frac{C}{1 - i\omega\tau}\right) \qquad (2)$$

Here ω_p is the plasma frequency, τ is the scattering time, and C is the expectation value of $\langle \cos\theta \rangle$ for carrier scattering angle θ. Carrier density is calculated from the plasma frequency according to

$$N = \frac{\varepsilon_0 \omega_p^2 m^*}{e^2} \qquad (3)$$

where m^* is the effective mass. The mobility can be calculated as

$$\mu = \frac{e^2 \tau}{m^*} \qquad (4)$$

The C parameter indicates carrier localization and may vary from 0 (Drude model) to -1 (fully localized). At a delay time of 10 ps, the Drude–Smith fit (solid red line in Figure 3) indicates a total carrier density of 2.8×10^{18} cm^{-3}, mobility of 49 cm^2 V^{-1} s^{-1}, and C parameter of -0.81. These values are similar to values of 4.0×10^{18} cm^{-3} and 31 cm^2 V^{-1} s^{-1} calculated using the peak photoconductivity in Figure 1b, which assumed nearly complete absorption of the incident photon flux within a depth of $\sim$120 nm. The similarity of the parameters calculated by two different methods provides confidence in the approach. The C parameter of -0.81 indicates significant backscattering, which is not surprising given the nanocrystalline composition of the film.

Diffusion Lengths in PbSe NC Thin Films. Diffusion length is a critical parameter that determines the ability to collect photoexcited minority carriers in solar cells, which often have depletion widths that are much smaller than the absorber thickness. To calculate the diffusion lengths of carriers in the PbSe films, an average lifetime $\langle \tau \rangle$ is calculated from $\langle \tau \rangle = \Sigma f_i \tau_i$, in which f_i is the steady-state population fraction of the decay.[58] This approach yields an estimate of the diffusion length according to $L = (\langle \tau \rangle \mu k_B T / q)^{1/2}$. Before reporting the results, three caveats about this should be stated. First, because TRTS is a local probe of conductivity, the diffusion lengths derived from these measurements should be understood as estimates: real devices are more sensitive to imperfections in film morphology and thus are likely to show suppressed carrier diffusion from lower effective mobilities.[59] Second, these measurements were performed on 5.5 nm PbSe NCs. Although the findings reported here are relevant to NC photovoltaics, most solar cells use smaller PbSe or PbS NCs, which typically show lower mobilities in devices (10^{-2}–10^{-4} cm^2 V^{-1} s^{-1}). Third, the electron and hole are treated as equal contributors to conductivity, meaning that they have equal mobilities since they are photoexcited in equal numbers. This is likely a reasonable assumption for PbSe, since similar mobilities have been measured for electrons and holes in ambipolar PbSe and PbS devices.[49] However, it may not apply to other
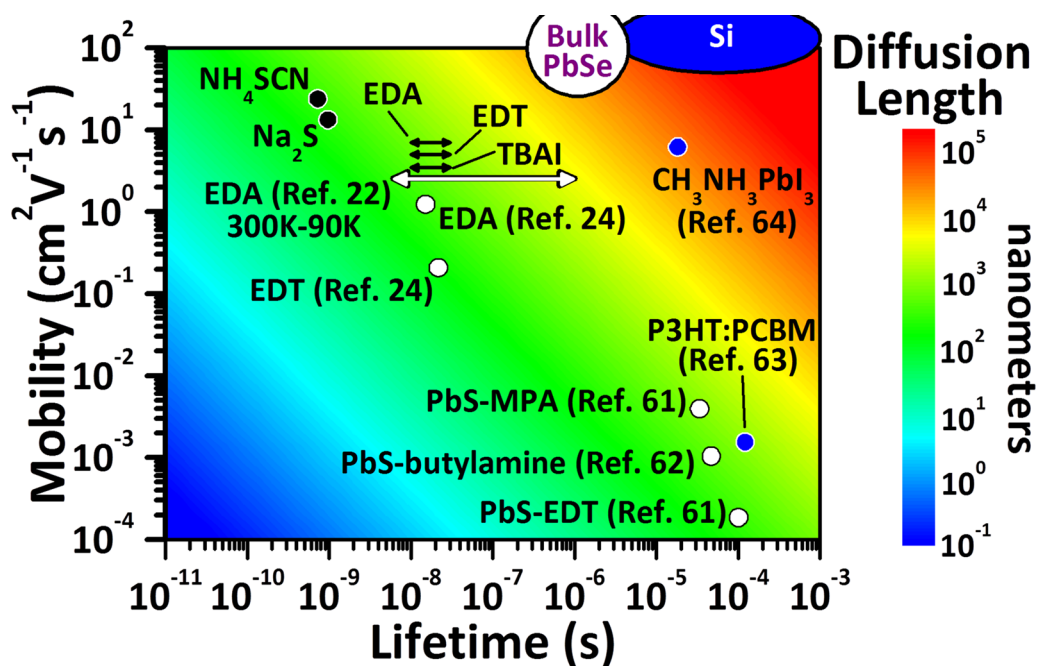
Figure 4. Contour plot of the diffusion length as a function of carrier mobility and lifetime. The samples studied in this work are labeled on the plot with black dots or black arrows. EDA, EDT, and TBAI arrows showing the range of diffusion lengths are offset slightly from measured values for visual clarity. Reference regions for bulk PbSe[43,60] microwave photoconductivity measurements[22,24] and previously measured lead chalcogenide photovoltaic materials are shown as white dots or arrows.[61,62] Additionally, blue dots indicate other photovoltaic materials processed at low temperature, including organic photovoltaic blends[63] and organolead halide perovskites.[64] Supporting Information Figure S11 shows a similar figure with additional reference points.

semiconductors where electrons and holes have very different mobilities.

For NH$_4$SCN- ($\langle\tau\rangle$ = 610 ps) and Na$_2$S-exchanged samples ($\langle\tau\rangle$ = 880 ps), the diffusion lengths estimated using this method are 220 and 230 nm, respectively. These points are plotted with black dots on a generic contour plot of diffusion length as a function of mobility and lifetime in Figure 4. Due to the uncertainty of the lifetime of EDA-, EDT-, and TBAI-treated samples, we calculated a range of diffusion lengths based on reasonable lifetimes, which are presented with black double arrows in Figure 4. Although PbSe NCs in solution show long photoluminescence decay times (>1 μs), solid films show shortened photoluminescence lifetimes from 30 to 300 ns.[65] Photoconductivity decay rates are generally shorter in ligand-exchanged NCs when measured using microwave conductivity,[24] so we provide a band of estimates of the diffusion length in Figure 4 with values of $\langle\tau\rangle$ from 10 to 30 ns, resulting in estimated diffusion lengths of 410−700 nm for EDA, 390−670 nm for EDT, and 300−570 nm for TBAI. Thus, under reasonable assumptions of the long time decay, estimated diffusion lengths in EDA, EDT, and TBAI range from 1.5 to 3 times longer than NH$_4$SCN and Na$_2$S. In fact, the range of effective lifetimes shown here may be conservative: transient absorption measurements of trap-to-band features of PbS NC films show lifetimes of >10 μs.[61] Without time-correlated conductivity measurements, however, it remains difficult to determine if carriers in such trap bands are contributing to photocurrent.

Several other literature results for PbE materials obtained by various methods are plotted in Figure 4. In most cases measured thus far, including in this work, the diffusion length for these materials falls, regardless of mobility, into a band of roughly 100−1000 nm. This "mobility-invariant" regime has been addressed previously by invoking trap states, some of which have been identified, as the mechanism for reduced diffusion lengths.[14,66] In this model, samples with high mobility (*i.e.*, diffusivity) find recombination sites faster, but diffusion lengths are fixed primarily by the density of trap states. We confirm from our measurements of PbSe NC solids that current chemical processing that enhances mobility in NC solids is accompanied by reduced photocarrier lifetime. Our data suggest that the effects of high diffusivity from enhanced interparticle coupling can be *more than offset* by rapid decay dynamics, resulting in shorter diffusion length. Much effort has driven NC ligand exchange to closer distances with lower interparticle barriers, leading even to fusion of neighboring particles.[29,32,37,38,67] We conclude from TRTS measurements that enhanced interparticle coupling has so far come at even greater cost of excited state lifetime.

This distinction has substantial consequences in the performance of different devices. NC-based FETs, which typically operate in accumulation, are majority-carrier devices in which excited-state carrier lifetime does not determine device mobility, which is improved by interparticle coupling. Although the

number and depth of trap states may constrain mobility, high-mobility NC FETs have been fabricated primarily through reduction of traps and trap-filling by manipulating the Fermi level or quasi-Fermi level such that extended "band-like" transport levels are accessible.[28,29,32,67,68] On the contrary, high-performance NC photovoltaics require the extraction of photoexcited minority carriers for maximum efficiency. Diffusion length is a critical parameter for controlling the collection probability of photo-generated carriers in a photovoltaic, and reduction in the diffusion length diminishes performance. Changes of carrier mobility and changes of photo-excited carrier lifetime are equally consequential for photovoltaics.

CONCLUSIONS

TRTS measurements of ligand-exchanged PbSe NC films allow empirical measurement of the photoexcited charge carrier mobility and lifetime, which enables an estimation of the diffusion length of photoexcited carriers in PbSe NC solids. PbSe NC films with NH_4SCN, Na_2S, EDA, EDT, and TBAI ligand exchanges were evaluated because of the reported performance of electronic and photovoltaic devices made from such films. The NH_4SCN and Na_2S exchanges exhibited the highest mobilities but suffered from rapid decays of the photoconductivity. The lifetime behavior of EDA-, EDT-, and TBAI-treated samples is distinctly different: although these samples contain subnanosecond transients, approximately one-third of the carriers exhibit a lifetime beyond 10 ns. As a result, we estimate diffusion lengths of lower-mobility samples that are greater than those of higher-mobility NC solids. These results provide a physical basis for understanding the prevailing strategies for enhancing the performance of NC photovoltaics and FETs.

MATERIALS AND METHODS

Materials. A 19 mm × 19 mm × 0.25 mm quartz coverglass used as the substrate for terahertz measurements was purchased from Chemglass. Home-built air-free sample cells were used to encapsulate samples for measurement within 1 in. sapphire windows (Rayotech) separated by a Viton O-ring. To perform frequency-resolved measurements, a thicker substrate (3/16 in. quartz, GM Associates) was used to space internal reflections of the substrate further apart in time. Oleic acid (90%), trioctylphosphine (90%), (3-mercaptopropyltrimethoxy)-silane (MPTS, 95%), diphenylphosphine (98%), selenium pellets (99.999%), EDA (99.5%), lead oxide (99.999%), and EDT (>98%) were purchased from Sigma-Aldrich. Octadecene (90%), NH_4SCN (99%+), and TBAI (98%) were purchased from Acros. Na_2S (anhydrous) was purchased from Alfa Aesar. NH_4SCN was recrystallized with anhydrous alcohol before use. Solvents were either purchased anhydrous or dried following standard methods.

Nanocrystal Synthesis. PbSe NCs were synthesized using a modified version of literature syntheses, which was specifically reoptimized for different batches of trioctylphosphine and diphenylphosphine based on the desired size.[69,70] For 5.5 nm PbSe NCs, 2.67 g of PbO was dissolved in 9 mL of oleic acid and 60 mL of octadecene at 120 °C under vacuum for 1 h. After turning clear, the solution was heated to 180 °C, whereupon 24 mL of 1 M Se in trioctylphosphine solution mixed with 207 μL of diphenylphosphine was rapidly injected. The reaction temperature was maintained at 160 °C for 20 min, then cooled and transferred into a nitrogen glovebox. Anhydrous purification was performed by precipitating with ethanol. The particles were redispersed in hexanes and precipitated two further times. Finally, the samples were dispersed in anhydrous octane at 50−100 mg/mL to fabricate films for spin-coating.

Electron Microscopy. Transmission electron microscopy was performed using a JEOL 2100 microscope operated at 200 keV. Scanning electron microscopy was performed using a JEOL 7500 microscope operated at 5 keV.

Deposition and Ligand Exchange. All substrates used for film deposition were treated with MPTS following literature procedures.[71] Two slightly different methods were used for ligand exchanges in this work. For NH_4SCN, Na_2S, TBAI, and EDT all procedures were performed sequentially directly on a spin-coater. First, two drops of a concentrated solution of NCs in octane was cast on the substrate, which was spun at 800 rpm for 1 min. Then six drops of ligand exchange solution (10 mg/mL NH_4SCN in acetonitrile, 10 mg/mL TBAI in methanol, 0.5 M Na_2S in methanol, 0.1 M EDT in acetonitrile) was placed on the substrate for 30 s (or 3 min for EDT), then spun off. Six drops of either clean acetonitrile or clean methanol (same as the ligand exchange solvent) was cast on the samples, left for 30 s, then spun off, followed by a similar rinse with octane. To make thicker films, this procedure was repeated 3−9 times. To prepare EDA-exchanged films, the ligand exchange step in the above sequence was replaced with a 1 h soak in 1 M EDA in methanol, to maintain better consistency with previous reports.[17]

Absorption Spectroscopy. UV−vis−NIR measurements were performed using a Cary 5000 absorption spectrometer. Mid-IR measurements were performed using a model 6700 Fourier transform infrared spectrometer (FTIR, Thermo Fisher). Solution-phase measurements were performed using a small amount of sample dissolved in tetrachloroethylene.

Van der Pauw Measurements. Gold contacts forming the corners of a 5 mm square were deposited on the films by thermal evaporation. Using these contacts, van der Pauw measurements were performed using an MMR H-50 controller. Hall measurements, which produced reliable values only for the NH_4SCN-exchanged sample, were measured in the same configuration using a 0.5 T fixed magnet.

Atomic Force Microscopy. Atomic force microscopy (AFM) measurements were performed to obtain film thicknesses using an Asylum Research AFM in tapping (ac) mode.

Terahertz Spectroscopy. TRTS was performed using a configuration described elsewhere.[15,16] Briefly, samples were excited with a 720 nm pump pulse, then probed at various delay times with THz radiation generated and detected using ZnTe nonlinear crystals. For average TRTS conductivity measurements, the change in transmission upon chopped photoexcitation was normalized by the nonphotoexcited signal to determine $\Delta E/E_{ref}$. The repetition rate was 1 kHz. The pump power was varied from 1 to 190 μJ/cm^2 per pulse for power-dependent studies. The power for studies highlighted in this work was 7.6 μJ/cm^2 per pulse for all but the NH_4SCN-exchanged sample, which was excited at 6.9 μJ/cm^2 per pulse. For frequency-resolved studies, the THz time-domain waveform was Fourier-transformed into a frequency space covering 0.4−1.5 THz.

Conflict of Interest: The authors declare no competing financial interest.

Supporting Information Available: Additional spectroscopy, derivations, electron microscopy, AFM, and further comparative data are available free of charge *via* the Internet at http://pubs.acs.org.

REFERENCES AND NOTES

1. Ridley, B. A. All-Inorganic Field Effect Transistors Fabricated by Printing. *Science* **1999**, *286*, 746–749.

2. Talapin, D. V.; Murray, C. B. PbSe Nanocrystal Solids for n- and p-Channel Thin Film Field-Effect Transistors. *Science* **2005**, *310*, 86–89.

3. Kim, D. K.; Lai, Y.; Diroll, B. T.; Murray, C. B.; Kagan, C. R. Flexible and Low-Voltage Integrated Circuits Constructed from High-Performance Nanocrystal Transistors. *Nat. Commun.* **2012**, *3*, 1216.

4. Chung, D. S.; Lee, J.-S.; Huang, J.; Nag, A.; Ithurria, S.; Talapin, D. V. Low Voltage, Hysteresis Free, and High Mobility Transistors from All-Inorganic Colloidal Nanocrystals. *Nano Lett.* **2012**, *12*, 1813–1820.

5. McDonald, S. A.; Konstantatos, G.; Zhang, S.; Cyr, P. W.; Klem, E. J. D.; Levina, L.; Sargent, E. H. Solution-Processed PbS Quantum Dot Infrared Photodetectors and Photovoltaics. *Nat. Mater.* **2005**, *4*, 138–142.

6. Konstantatos, G.; Howard, I.; Fischer, A.; Hoogland, S.; Clifford, J.; Klem, E.; Levina, L.; Sargent, E. H. Ultrasensitive Solution-Cast Quantum Dot Photodetectors. *Nature* **2006**, *442*, 180–183.

7. Keuleyan, S.; Lhuillier, E.; Brajuskovic, V.; Guyot-Sionnest, P. Mid-infrared HgTe Colloidal Quantum Dot Photodetectors. *Nat. Photonics* **2011**, *5*, 489–493.

8. Colvin, V. L.; Schlamp, M. C.; Alivisatos, A. P. Light-Emitting Diodes Made from Cadmium Selenide Nanocrystals and a Semiconducting Polymer. *Nature* **1994**, *370*, 354–357.

9. Sun, L.; Choi, J. J.; Stachnik, D.; Bartnik, A. C.; Hyun, B.-R.; Malliaras, G. G.; Hanrath, T.; Wise, F. W. Bright Infrared Quantum-Dot Light-Emitting Diodes through Inter-Dot Spacing Control. *Nat. Nanotechnol.* **2012**, *7*, 369–373.

10. Kim, T.-H.; Cho, K.-S.; Lee, E. K.; Lee, S. J.; Chae, J.; Kim, J. W.; Kim, D. H.; Kwon, J.-Y.; Amaratunga, G.; Lee, S. Y.; Choi, B. L.; Kuk, Y.; Kim, J. M.; Kim, K. Full-Colour Quantum Dot Displays Fabricated by Transfer Printing. *Nat. Photonics* **2011**, *5*, 176–182.

11. Gur, I.; Fromer, N. A.; Geier, M. L.; Alivisatos, A. P. Air-Stable All-Inorganic Nanocrystal Solar Cells Processed from Solution. *Science* **2005**, *310*, 462–465.

12. Talapin, D. V.; Lee, J.-S.; Kovalenko, M. V.; Shevchenko, E. V. Prospects of Colloidal Nanocrystals for Electronic and Optoelectronic Applications. *Chem. Rev.* **2010**, *110*, 389–458.

13. Chuang, C.-H. M.; Brown, P. R.; Bulović, V.; Bawendi, M. G. Improved Performance and Stability in Quantum Dot Solar Cells through Band Alignment Engineering. *Nat. Mater.* **2014**, *13*, 796–801.

14. Zhitomirsky, D.; Voznyy, O.; Levina, L.; Hoogland, S.; Kemp, K. W.; Ip, A. H.; Thon, S. M.; Sargent, E. H. Engineering Colloidal Quantum Dot Solids within and beyond the Mobility-Invariant Regime. *Nat. Commun.* **2014**, *5*, 3803.

15. Baxter, J. B.; Schmuttenmaer, C. A. Time-Resolved Terahertz Spectroscopy and Terahertz Emission Spectroscopy. In *Terahertz Specotroscopy: Principles and Applications*; Dexheimer, S. L., Ed.; CRC Press: Boca Raton, FL, 2007; pp 73−118.

16. Baxter, J. B.; Guglietta, G. W. Terahertz Spectroscopy. *Anal. Chem.* **2011**, *83*, 4342–4368.

17. Murphy, J. E.; Beard, M. C.; Nozik, A. J. Time-Resolved Photoconductivity of PbSe Nanocrystal Arrays. *J. Phys. Chem. B* **2006**, *110*, 25455–25461.

18. Beard, M. C.; Turner, G. M.; Murphy, J. E.; Micic, O. I.; Hanna, M. C.; Nozik, A. J.; Schmuttenmaer, C. A. Electronic Coupling in InP Nanoparticle Arrays. *Nano Lett.* **2003**, *3*, 1695–1699.

19. Turner, G. M.; Beard, M. C.; Schmuttenmaer, C. A. Carrier Localization and Cooling in Dye-Sensitized Nanocrystalline Titanium Dioxide. *J. Phys. Chem. B* **2002**, *106*, 11716–11719.

20. Baxter, J. B.; Schmuttenmaer, C. A. Conductivity of ZnO Nanowires, Nanoparticles, and Thin Films using Time-Resolved Terahertz Spectroscopy. *J. Phys. Chem. B* **2006**, *110*, 25229–25239.

21. Hendry, E.; Koeberg, M.; Wang, F.; Zhang, H.; de Mello Donegá, C.; Vanmaekelbergh, D.; Bonn, M. Direct Observation of Electron-to-Hole Energy Transfer in CdSe Quantum Dots. *Phys. Rev. Lett.* **2006**, *96*, 057408.

22. Talgorn, E.; Gao, Y.; Aerts, M.; Kunneman, L. T.; Schins, J. M.; Savenije, T. J.; van Huis, M. A.; van der Zant, H. S. J.; Houtepen, A. J.; Siebbeles, L. D. A. Unity Quantum Yield of Photogenerated Charges and Band-like Transport in Quantum-Dot Solids. *Nat. Nanotechnol.* **2011**, *6*, 733–739.

23. Talgorn, E.; de Vries, M. A.; Siebbeles, L. D. A.; Houtepen, A. J. Photoconductivity Enhancement in Multilayers of CdSe and CdTe Quantum Dots. *ACS Nano* **2011**, *5*, 3552–3558.

24. Gao, Y.; Aerts, M.; Sandeep, C. S. S.; Talgorn, E.; Savenije, T. J.; Kinge, S.; Siebbeles, L. D. A.; Houtepen, A. J. Photoconductivity of PbSe Quantum-Dot Solids: Dependence on Ligand Anchor Group and Length. *ACS Nano* **2012**, *6*, 9606–9614.

25. Vanderhoef, L. R.; Azad, A. K.; Bomberger, C. C.; Chowdhury, D. R.; Chase, D. B.; Taylor, A. J.; Zide, J. M. O.; Doty, M. F. Charge Carrier Relaxation Processes in TbAs Nano-inclusions in GaAs Measured by Optical-Pump THz-Probe Transient Absorption Spectroscopy. *Phys. Rev. B* **2014**, *89*, 045418.

26. Sandeep, C. S. S.; Azpiroz, J. M.; Evers, W. H.; Boehme, S. C.; Moreels, I.; Kinge, S.; Siebbeles, L. D. A.; Infante, I.; Houtepen, A. J. Epitaxially Connected PbSe Quantum-Dot Films: Controlled Neck Formation and Optoelectronic Properties. *ACS Nano* **2014**, *8*, 11499–11511.

27. Fafarman, A. T.; Koh, W.; Diroll, B. T.; Kim, D. K.; Ko, D.-K.; Oh, S. J.; Ye, X.; Doan-Nguyen, V.; Crump, M. R.; Reifsnyder, D. C.; Murray, C. B.; Kagan, C. R. Thiocyanate-Capped Nanocrystal Colloids: Vibrational Reporter of Surface Chemistry and Solution-Based Route to Enhanced Coupling in Nanocrystal Solids. *J. Am. Chem. Soc.* **2011**, *133*, 15753–15761.

28. Choi, J.-H.; Fafarman, A. T.; Oh, S. J.; Ko, D.-K.; Kim, D. K.; Diroll, B. T.; Muramoto, S.; Gillen, J. G.; Murray, C. B.; Kagan, C. R. Bandlike Transport in Strongly Coupled and Doped Quantum Dot Solids: A Route to High-Oerformance Thin-Film Electronics. *Nano Lett.* **2012**, *12*, 2631–2638.

29. Oh, S. J.; Berry, N. E.; Choi, J.-H.; Gaulding, E. A.; Lin, H.; Paik, T.; Diroll, B. T.; Muramoto, S.; Murray, C. B.; Kagan, C. R. Designing High-Performance PbS and PbSe Nanocrystal Electronic Devices through Stepwise, Post-Synthesis, Colloidal Atomic Layer Deposition. *Nano Lett.* **2014**, *14*, 1559–1566.

30. Nag, A.; Kovalenko, M. V.; Lee, J.-S.; Liu, W.; Spokoyny, B.; Talapin, D. V. Metal-Free Inorganic Ligands for Colloidal Nanocrystals: S^{2-}, HS^-, Se(2−), HSe^-, Te^{2-}, HTe^-, TeS_3^{2-}, OH^-, and NH_2^- as Surface Ligands. *J. Am. Chem. Soc.* **2011**, *133*, 10612–10620.

31. Zhang, H.; Hu, B.; Sun, L.; Hovden, R.; Wise, F. W.; Muller, D. A.; Robinson, R. D. Surfactant Ligand Removal and Rational Fabrication of Inorganically Connected Quantum Dots. *Nano Lett.* **2011**, *11*, 5356–5361.

32. Liu, Y.; Tolentino, J.; Gibbs, M.; Ihly, R.; Perkins, C. L.; Liu, Y.; Crawford, N.; Hemminger, J. C.; Law, M. PbSe Quantum Dot Field-Effect Transistors with Air-Stable Electron Mobilities above 7 cm^2 V^{-1} s^{-1}. *Nano Lett.* **2013**, *13*, 1578–1587.

33. Luther, J. M.; Law, M.; Beard, M. C.; Song, Q.; Reese, M. O.; Ellingson, R. J.; Nozik, A. J. Schottky Solar Cells Based on Colloidal Nanocrystal Films. *Nano Lett.* **2008**, *8*, 3488–3492.

34. Ip, A. H.; Thon, S. M.; Hoogland, S.; Voznyy, O.; Zhitomirsky, D.; Debnath, R.; Levina, L.; Rollny, L. R.; Carey, G. H.; Fischer, A.; *et al*. Hybrid Passivated Colloidal Quantum Dot Solids. *Nat. Nanotechnol.* **2012**, *7*, 577–582.

35. Williams, K. J.; Tisdale, W. A.; Leschkies, K. S.; Haugstad, G.; Norris, D. J.; Aydil, E. S.; Zhu, X.-Y. Strong Electronic Coupling in Two-Dimensional Assemblies of Colloidal PbSe Quantum Dots. *ACS Nano* **2009**, *3*, 1532–1538.

36. Schapotschnikow, P.; van Huis, M. A.; Zandbergen, H. W.; Vanmaekelbergh, D.; Vlugt, T. J. H. Morphological Transformations and Fusion of PbSe Nanocrystals Studied Using Atomistic Simulations. *Nano Lett.* **2010**, *10*, 3966–3971.

37. Baumgardner, W. J.; Whitham, K.; Hanrath, T. Confined-but-Connected Quantum Solids *via* Controlled Ligand Displacement. *Nano Lett.* **2013**, *13*, 3225–3231.

38. Boneschanscher, M. P.; Evers, W. H.; Geuchies, J. J.; Altantzis, T.; Goris, B.; Rabouw, F. T.; van Rossum, S. A. P.; van der Zant, H. S. J.; Siebbeles, L. D. A.; Van Tendeloo, G.; et al. Long-Range Orientation and Atomic Attachment of Nanocrystals in 2D Honeycomb Superlattices. *Science* **2014**, *344*, 1377–1380.

39. Guglietta, G. W.; Choudhury, K. R.; Caspar, J. V.; Baxter, J. B. Employing Time-Resolved Terahertz Spectroscopy to Analyze Carrier Dynamics in Thin-Film $Cu_2ZnSn(S,Se)_4$ Absorber Layers. *Appl. Phys. Lett.* **2014**, *104*, 253901.

40. Jepsen, P. U.; Cooke, D. G.; Koch, M. Terahertz Spectroscopy and Imaging - Modern Techniques and Applications. *Laser Photonics Rev.* **2011**, *5*, 124–166.

41. Mics, Z.; D'Angio, A.; Jensen, S. A.; Bonn, M.; Turchinovich, D. Density-Dependent Electron Scattering in Photoexcited GaAs in Strongly Diffusive Regime. *Appl. Phys. Lett.* **2013**, *102*, 231120.

42. Moreels, I.; Lambert, K.; De Muynck, D.; Vanhaecke, F.; Poelman, D.; Martins, J. C.; Allan, G.; Hens, Z. Composition and Size-Dependent Extinction Coefficient of Colloidal PbSe Quantum Dots. *Chem. Mater.* **2007**, *19*, 6101–6106.

43. Allgaier, R.; Scanlon, W. Mobility of Electrons and Holes in PbS, PbSe, and PbTe between Room Temperature and 4.2 K. *Phys. Rev.* **1958**, *111*, 1029–1037.

44. Kang, I.; Wise, F. W. Electronic Structure and Optical Properties of PbS and PbSe Quantum Dots. *J. Opt. Soc. Am. B* **1997**, *14*, 1632–1646.

45. Ponseca, C. S.; Savenije, T. J.; Abdellah, M.; Zheng, K.; Yartsev, A.; Pascher, T.; Harlang, T.; Chabera, P.; Pullerits, T.; Stepanov, A.; Wolf, J.-P.; Sundström, V. Organometal Halide Perovskite Solar Cell Materials Rationalized: Ultrafast Charge Generation, High and Microsecond-Long Balanced Mobilities, and Slow Recombination. *J. Am. Chem. Soc.* **2014**, *136*, 5189–5192.

46. Leijtens, T.; Stranks, S. D.; Eperon, G. E.; Lindblad, R.; Johansson, E. M. J.; McPherson, I. J.; Rensmo, H.; Ball, J. M.; Lee, M. M.; Snaith, H. J. Electronic Properties of Meso-Superstructured and Planar Organometal Halide Perovskite Films: Charge Trapping, Photodoping, and Carrier Mobility. *ACS Nano* **2014**, *8*, 7147–7155.

47. Rosen, E. L.; Buonsanti, R.; Llordes, A.; Sawvel, A. M.; Milliron, D. J.; Helms, B. A. Exceptionally Mild Reactive Stripping of Native Ligands from Nanocrystal Surfaces by Using Meerwein's Salt. *Angew. Chem., Int. Ed.* **2012**, *51*, 684–649.

48. Law, M.; Luther, J. M.; Song, Q.; Hughes, B. K.; Perkins, C. L.; Nozik, A. J. Structural, Optical, and Electrical Properties of PbSe Nanocrystal Solids Treated Thermally or with Simple Amines. *J. Am. Chem. Soc.* **2008**, *130*, 5974–5985.

49. Luther, J. M.; Law, M.; Song, Q.; Perkins, C. L.; Beard, M. C.; Nozik, A. J. Structural, Optical, and Electrical Properties of Self-Assembled Films of PbSe Nanocrystals Treated with 1,2-Ethanedithiol. *ACS Nano* **2008**, *2*, 271–80.

50. Oh, S. J.; Wang, Z.; Berry, N. E.; Choi, J.-H.; Zhao, T.; Gaulding, E. A.; Paik, T.; Lai, Y.; Murray, C. B.; Kagan, C. R. Engineering Charge Injection and Charge Transport for High Performance PbSe Nanocrystal Thin Film Devices and Circuits. *Nano Lett.* **2014**, *14*, 6210–6216.

51. Marshall, J. M. Carrier Diffusion in Amorphous Semiconductors. *Rep. Prog. Phys.* **1983**, *46*, 1235–1282.

52. Gao, Y.; Talgorn, E.; Aerts, M.; Trinh, M. T.; Schins, J. M.; Houtepen, A. J.; Siebbeles, L. D. A. Enhanced Hot-Carrier Cooling and Ultrafast Spectral Diffusion in Strongly Coupled PbSe Quantum-Dot Solids. *Nano Lett.* **2011**, *11*, 5471–5476.

53. Gao, Y.; Suchand Sandeep, C. S.; Schins, J. M.; Houtepen, A. J.; Siebbeles, L. D. A. Disorder Strongly Enhances Auger Recombination in Conductive Quantum-Dot Solids. *Nat. Commun.* **2013**, *4*, 2329.

54. Cooke, D.; MacDonald, A.; Hryciw, A.; Wang, J.; Li, Q.; Meldrum, A.; Hegmann, F. Transient Terahertz Conductivity in Photoexcited Silicon Nanocrystal Films. *Phys. Rev. B* **2006**, *73*, 193311.

55. Titova, L. V.; Cocker, T. L.; Cooke, D. G.; Wang, X.; Meldrum, A.; Hegmann, F. A. Ultrafast Percolative Transport Dynamics in Silicon Nanocrystal Films. *Phys. Rev. B* **2011**, *83*, 085403.

56. Lloyd-Hughes, J.; Jeon, T.-I. A Review of the Terahertz Conductivity of Bulk and Nano-Materials. *J. Infrared, Millimeter, Terahertz Waves* **2012**, *33*, 871–925.

57. Smith, N. Classical Generalization of the Drude Formula for the Optical Conductivity. *Phys. Rev. B* **2001**, *64*, 155106.

58. Lakowicz, J. *Principles of Fluorescence Spectroscopy*, 3rd ed.; Springer: New York, 2006; pp 98−157.

59. Zhitomirsky, D.; Voznyy, O.; Hoogland, S.; Sargent, E. H. Measuring Charge Carrier Diffusion in Coupled Colloidal Quantum Dot Solids. *ACS Nano* **2013**, *7*, 5282–5290.

60. Coates, D. G.; Lawson, W. D.; Prior, A. C. Single Crystal Photoconductive Detectors in Lead Selenide. *J. Electrochem. Soc.* **1961**, *108*, 1038–1042.

61. Jeong, K. S.; Tang, J.; Liu, H.; Kim, J.; Schaefer, A. W.; Kemp, K.; Levina, L.; Wang, X.; Hoogland, S.; Debnath, R.; et al. Enhanced Mobility-Lifetime Products in PbS Colloidal Quantum Dot Photovoltaics. *ACS Nano* **2012**, *6*, 89–99.

62. Johnston, K. W.; Pattantyus-Abraham, A. G.; Clifford, J. P.; Myrskog, S. H.; Hoogland, S.; Shukla, H.; Klem, E. J. D.; Levina, L.; Sargent, E. H. Efficient Schottky-Quantum-Dot Photovoltaics: The Roles of Depletion, Drift, and Diffusion. *Appl. Phys. Lett.* **2008**, *92*, 122111.

63. Garcia-Belmonte, G.; Munar, A.; Barea, E. M.; Bisquert, J.; Ugarte, I.; Pacios, R. Charge Carrier Mobility and Lifetime of Organic Bulk Heterojunctions Analyzed by Impedance Spectroscopy. *Org. Electron.* **2008**, *9*, 847–851.

64. Wehrenfennig, C.; Eperon, G. E.; Johnston, M. B.; Snaith, H. J.; Herz, L. M. High Charge Carrier Mobilities and Lifetimes in Organolead Trihalide Perovskites. *Adv. Mater.* **2014**, *26*, 1584–1589.

65. Kovalenko, M. V.; Talapin, D. V.; Loi, M. A.; Cordella, F.; Hesser, G.; Bodnarchuk, M. I.; Heiss, W. Quasi-Seeded Growth of Ligand-Tailored PbSe Nanocrystals through Cation-Exchange-Mediated Nucleation. *Angew. Chem., Int. Ed.* **2008**, *47*, 3029–3033.

66. Carey, G. H.; Kramer, I. J.; Kanjanaboos, P.; Moreno-Bautista, G.; Voznyy, O.; Rollny, L.; Tang, J. A.; Hoogland, S.; Sargent, E. H. Electronically Active Impurities in Colloidal Quantum Dot Solids. *ACS Nano* **2014**, *8*, 11763–11769.

67. Oh, S. J.; Berry, N. E.; Choi, J.-H.; Gaulding, E. A.; Paik, T.; Hong, S.-H.; Murray, C. B.; Kagan, C. R. Stoichiometric Control of Lead Chalcogenide Nanocrystal Solids to Enhance their Electronic and Optoelectronic Device Performance. *ACS Nano* **2013**, *7*, 2413–2421.

68. Lee, J.-S.; Kovalenko, M. V.; Huang, J.; Chung, D. S.; Talapin, D. V. Band-like Transport, High Electron Mobility and High Photoconductivity in All-Inorganic Nanocrystal Arrays. *Nat. Nanotechnol.* **2011**, *6*, 348–352.

69. Yu, W. W.; Falkner, J. C.; Shih, B. S.; Colvin, V. L. Preparation and Characterization of Monodisperse PbSe Semiconductor Nanocrystals in a Noncoordinating Solvent. *Chem. Mater.* **2004**, *16*, 3318–3322.

70. Steckel, J. S.; Yen, B. K. H.; Oertel, D. C.; Bawendi, M. G. On the Mechanism of Lead Chalcogenide Nanocrystal Formation. *J. Am. Chem. Soc.* **2006**, *128*, 13032–13033.

71. Pallavicini, P.; Dacarro, G.; Galli, M.; Patrini, M. Spectroscopic Evaluation of Surface Functionalization Efficiency in the Preparation of Mercaptopropyltrimethoxysilane Self-Assembled Monolayers on Glass. *J. Colloid Interface Sci.* **2009**, *332*, 432–438.